Title

Contrasting Effects of Inhibitors Li^{+} and Be^{2+} on Catalytic Cycle of Glycogen Synthase Kinase-3β.

Journal

The journal of physical chemistry. B, 125(33)

ISSN

1520-6106

Authors

Reilley, David J
Arraf, Zaher
Alexandrova, Anastassia N

Publication Date

2021-08-01

DOI

10.1021/acs.jpcb.1c05099

Peer reviewed

Contrasting Effects of Inhibitors Li^+ and Be^{2+} on Catalytic Cycle of Glycogen Synthase Kinase-3β

David J. Reilley,[†] Zaher Arraf,[*,‡] Anastassia N. Alexandrova[**,†,§]

[†] Department of Chemistry and Biochemistry, University of California, Los Angeles, Los Angeles, California 90095-1569, United States

[‡] Department of Education in Technology and Science, Technion-Israel Institute of Technology, 32000, Haifa, Israel

[§] California NanoSystems Institute, Los Angeles, California 90095-1569, United States

KEYWORDS: GSK-3β, Inhibition, Lithium, Beryllium, Chemical Calculations, QM/DMD, Molecular Dynamics

ABSTRACT: Ionic lithium shows rare effectiveness for treating bipolar disorder and is a promising drug for treating neurodegenerative diseases. Unfortunately, lithium suffers from significant drawbacks as a drug, mainly a narrow therapeutic window. Among the different targets of lithium, glycogen synthase kinase 3β (GSK-3β) might be the one responsible for its therapeutic effects. Developing alternative, selective inhibitors of this kinase could avoid lithium side effects, but efforts to do so have met little success so far. A detailed, atomistic understanding of Li^+ inhibition and a more detailed understanding of the phosphorylation reaction GSK-3β catalyzes would therefore facilitate the development of new drugs. In this study, we use extensive sampling of catalytic states with our mixed quantum-classical dynamics method QM/DMD and binding affinities from a competitive metal affinity (CMA) approach to fill out the atomic scale picture of Li^+ GSK-3β inhibition. We compare Li^+ action with Be^{2+}, another known inhibitor, and find our results in agreement with *in-vitro* kinetics studies. Ultimately, our simulations show that Li^+ inhibition is driven primarily by directly decreasing the reaction rate of the phosphorylation step, rather than reducing catalytic turnover through tight binding to different GSK-3β states like Be^{2+} inhibition. The effect of these metals derive from electrostatic differences and especially their smaller atomic radii compared to the native Mg^{2+} and thus provides insight for the development of GSK-3β inhibitors based on other paradigms.

Introduction: Glycogen synthase kinase-3β (GSK-3β) is an important therapeutic target for a wide range of neurological conditions. GSK-3β dysfunction is known or proposed to be implicated in bipolar disorder (BD), Parkinson's disease, epilepsy, and Alzheimer's disease (AD) (according to the prominent tau hyperphosphorylation hypothesis).[1–3] Consequentially, GSK-3β is an attractive target for inhibitors to treat these conditions,[4–7] and some have even entered clinical trials.[8] However, no recent efforts have yet passed, encountering problems with toxicity and efficacy.[9] GSK-3β is difficult to target selectively as it is highly homologous with related kinases, particularly mitogen-activated protein kinases (MAPKs), cyclin-dependent kinases (CDKs), and protein kinase C (PKC). This family of proteins all bind an ATP molecule alongside two Mg^{2+} ions at a site adjacent to a peptide/protein substrate binding channel (Figure 1A).[10] As the most conserved region between these proteins is the ATP binding site, a well-studied potential solution to this are allosteric inhibitors.[11,12] Although ATP non-competitive compounds can improve selectivity, their more subtle modes of binding and inhibition make them difficult to develop into effective drugs. Study of a past, and rare, successful therapeutic agent would be especially helpful in the design of new ones.

Lithium is one of the most effective treatments for BD, and evidence for its beneficial effects on other neurological conditions have recently been gathering. The metal has been used for its mood stabilizing effect for BD since its serendipitous discovery in 1949.[13] *In-vivo* and even clinical studies report some beneficial effects on AD pathology, but with conflicting results.[14,15] Li^+ therapeutic action is believed to be driven primarily through altering pro- and anti-apoptotic gene expression and GSK-3β inhibition.[16] Kinetic studies comparing Li^+ to Be^{2+}, another potent inhibitor, demonstrate that Li^+ binds non-competitively with ATP, just replacing one of the two native Mg^{2+} ions.[17,18] Remarkably, Li^+ has a limited effect on the activity of closely related CDK5, PKC, and MAPK.[1] Lithium does, however, have major drawbacks as a drug: a narrow therapeutic index, with therapeutic levels between 0.6 and 1.5 mEg/Lit,[19] and several side effects[20] – though it is specific, regarding altering activity of GSK-3β among other kinases, it clearly has other targets. An atomic-scale picture of GSK-3β activity and Li^+ inhibition would explain some of this behavior and aid the development of new, selective therapeutics without these drawbacks.

There have been many structural studies on related kinases and the biological effect of Li^+, but how the metal inhibits GSK-3β is not fully understood. Experimental and computational research on the related protein kinase A (PKA) has established a likely SN1 or SN2-like mechanism of phosphoryl transfer facilitated by a nearby aspartate residue acting as a base (Figure 1B).[21,22] Quantum mechanical (QM) calculations

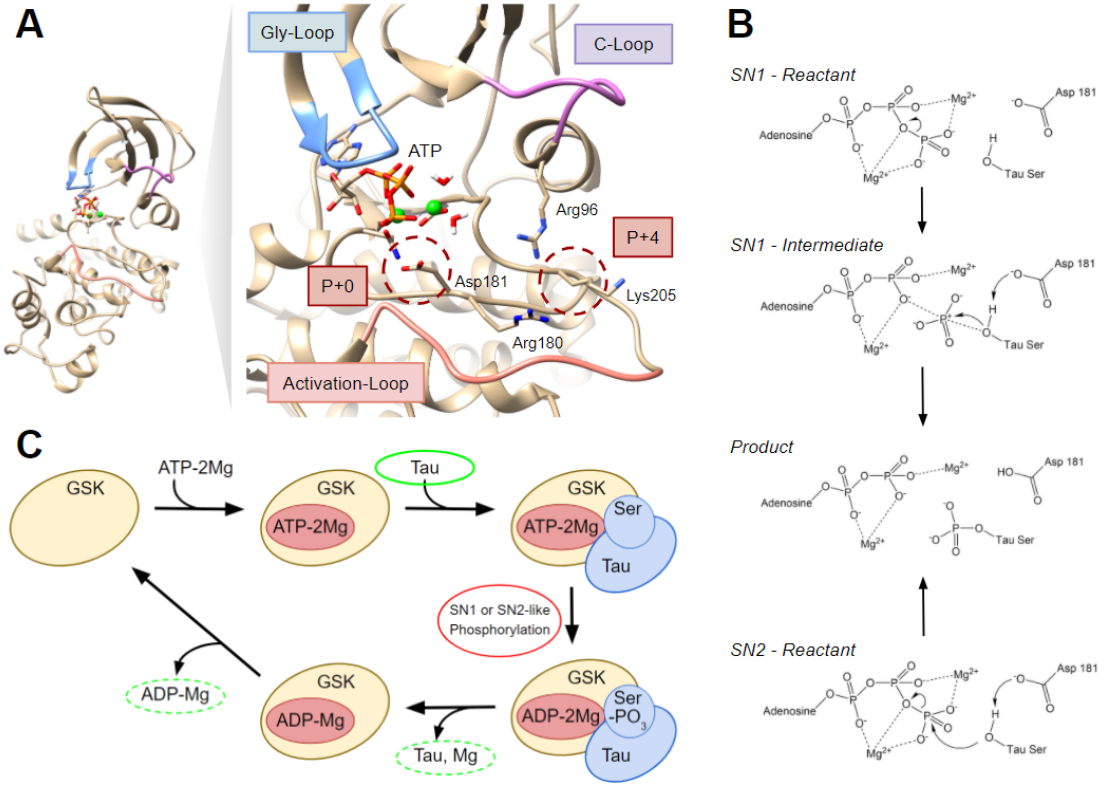

Figure 1: (A) Ribbon diagram of GSK-3β structure with insert showing the ATP binding site under the Gly-Loop (in blue) and the peptide/protein substrate binding channel, defined by the Gly-Loop, C-Loop (in purple) and Activation-Loop (in pink). The substrate serine or threonine residue binds at the P+0 site while a pre-phosphorylated residue binds at the P+4 site, held tightly by a series of charged residues (Arg96, Arg180, Lys205). (B) The dominant phosphorylation mechanism for GSK-3β based on studies of related kinases. The reaction proceeds by either an SN1 or SN2 path, with a nearby Asp181 residue acting as the base. (C) The catalytic cycle of GSK-3β. Li^+ and Be^{2+} binding could inhibit activity by directly increasing the phosphorylation reaction barrier (circled red) or by disrupting the binding of the substrate (tau in this study, circled solid green) or either the unbinding of the substrate or ADP complex (circled dashed green).

on small mimic complexes of the GSK-3β metal binding site suggest that Li^+ can replace Mg^{2+} in only the ATP-bound forms of the protein,[23] but truncated model systems like these do not take the full effect of the protein environment into account. Later dynamics simulations on GSK-3β indicate that Li^+ preferentially binds to one Mg^{2+} site but not the other.[24,25] However, these studies did not confirm their results by calculating thermodynamic quantities such as binding energies or reaction barriers, nor did they consider the role Li^+ could play in other steps of the catalytic cycle.

This computational study investigated the atomic-scale effect of Li^+ and Be^{2+} on each relevant step of the GSK-3β catalytic cycle. Metal inhibition could arise from a direct increase to the phosphorylation reaction barrier or disruption of the timely binding or detachment of other groups that could slow turnover: ATP, ADP, or the peptide substrate (Figure 1C). We employed the established QM/DMD method to study the structure of the ATP and ADP bound states of GSK-3β. This method combines QM calculations for appropriate treatment of the metal environment with discrete molecular dynamics simulations for rapid and extensive sampling of protein conformations. We also performed additional QM calculations to obtain binding affinities and phosphorylation reaction barriers based on the lowest energy structures identified by QM/DMD. We consider the effect of docking a tau protein fragment, a species implicated in AD, as an example substrate. We also identify structural differences between the native and Li^+ states that could serve as targets for future inhibitor development.

Theoretical Methods: This study began with dynamics simulations using the QM/DMD method.[26] This technique samples metalloprotein configurations using quantum mechanical (QM) electronic structure calculations (normally density functional theory) necessary to describe the metal and its coordination environment (referred to as the 'QM region') and discrete molecular dynamics (DMD)[27,28] to model the rest of the protein. Both methods treat an overlapping QM/DMD region which consists of species constituting the active site but not directly binding to the metal. This region enables inter-region geometric communication and mitigates discontinuity errors. QM/DMD has a strong record of successfully explaining a range of metalloenzyme behaviors. These include metal-dependent catalytic activity,[29,30] protein-metal binding affinity,[30,31] the effect of mutagenesis on structure,[32,33] and flexible docking of substrates.[34]

All of the QM calculations in this study were performed at the density functional theory (DFT) level using Turbomole (version 6.6).[35] The pure meta-GGA TPSS functional[36] was used with the D3 dispersion correction.[37] The metal was modeled with the triple-zeta basis set def2-TZVPP while all other atoms were treated with the double-zeta def2-SVP basis set.[38] A small basis set may result in some degree of basis set superposition error, but the large size of the QM regions (111-116 atoms) precluded any larger basis set. Regardless, this

level of theory has proven effective in previous studies, including for quantitative free energy comparisons.[30,31] Lastly, the Conductor-like Screen Model (COSMO)[39] with a constant dielectric of 20 was applied to approximate the partial screening and solvation effects in the partly buried active site. Any water molecules that directly coordinate to the metals were modeled explicitly. All QM calculations were performed to convergence withtin 1.0 x 10^{-7} Hartree or at least 100 SCF cycles to afford more sampling during QM/DMD simulations. All DMD phases in the QM/DMD simulations in this study were performed for 10,000 steps per iteration (roughly 0.5 ns). DMD operates with an implicit solvent through the appropriate potentials in its forcefield.

QM/DMD simulations were performed on all the catalytic forms of GSK-3β for each metal binding state with one exception. Attempts to dock a short peptide proxy for tau protein were unsuccessful due to the poor potentials for the pre-phosphorylated residue in DMD. Thus, the simulations only capture the ATP and ADP bound states of the protein without tau, which proves to be sufficient for the purposes of this study.

QM/DMD simulations were performed on the 8 total metal bound states of GSK-3β-ATP and GSK-3β-ADP. For the ADP form these include the Mg^{2+}, Li^{+}, and Be^{2+} states. In the case of the ATP form, as there are two metal binding sites, these include the $2Mg^{2+}$, $Li^{+}Mg^{2+}$, $Mg^{2+}Li^{+}$, $Be^{2+}Mg^{2+}$, and $Mg^{2+}Be^{2+}$ states. The first denoted metal represents the site closer to the ATP adenosine group while the second one represents the further site. Simulations were performed in 5 replicate QM/DMD trajectories for the native Mg^{2+} and Li^{+} containing states of the ATP form and 3 replicate trajectories for the other systems, i.e. a total of 30 simulations. Each trajectory was continued for 40 iterations, which roughly corresponds to 20 ns. Full rationalization of the construction of each system can be found in the supporting information.

The convergence of the QM/DMD simulations was achieved according to several benchmarks: the protein backbone RMSD, the DMD energy, and QM region energy. All QM/DMD simulations were converged by 40 iterations / ~ 20 ns by these metrics. The full convergence charts with respect to the three standards are shown in the supporting information.

Further optimization of the QM region was done to generate the structures for free energy and metal angular variance calculations. The ten QM regions for each system with the lowest unoptimized electronic energy were fully converged (when not already achieved) using the same level of theory as the QM calculations from QM/DMD. The free energy was then calculated for each with a harmonic frequency calculation. The structure with the lowest free energy was then selected as the representative minimum of each system.

Potential energy surface (PES) scans were performed to calculate the phosphorylation reaction barriers for the $2Mg^{2+}$, $Li^{+}Mg^{2+}$, and $Be^{2+}Mg^{2+}$ states of the protein. The two reaction coordinates were the distance between the O and H of the tau serine (from 0.8Å to 2.2Å), and the distance between O of the tau serine and the terminal P on ATP (from 1.4Å to 2.6Å), with a step of 0.1Å. The active spaces were truncated from the lowest energy QM optimized structures with a fragment of tau manually docked into these structured and truncated at the Cβ (capped with a hydrogen and with its position frozen in all calculations). Without full dynamics for the tau substrate, these constraints could introduce errors into the calculated energies and barriers, but full dynamics could not be obtained as explained above. Full details of the system construction are found in the supporting information. Once the PES were plotted, the stationary points were fully optimized with the same level of DFT theory as the QM calculations from QM/DMD with accompanying harmonic frequency calculations to obtain free energies for the reactant and product states as well as any intermediates and transition states.

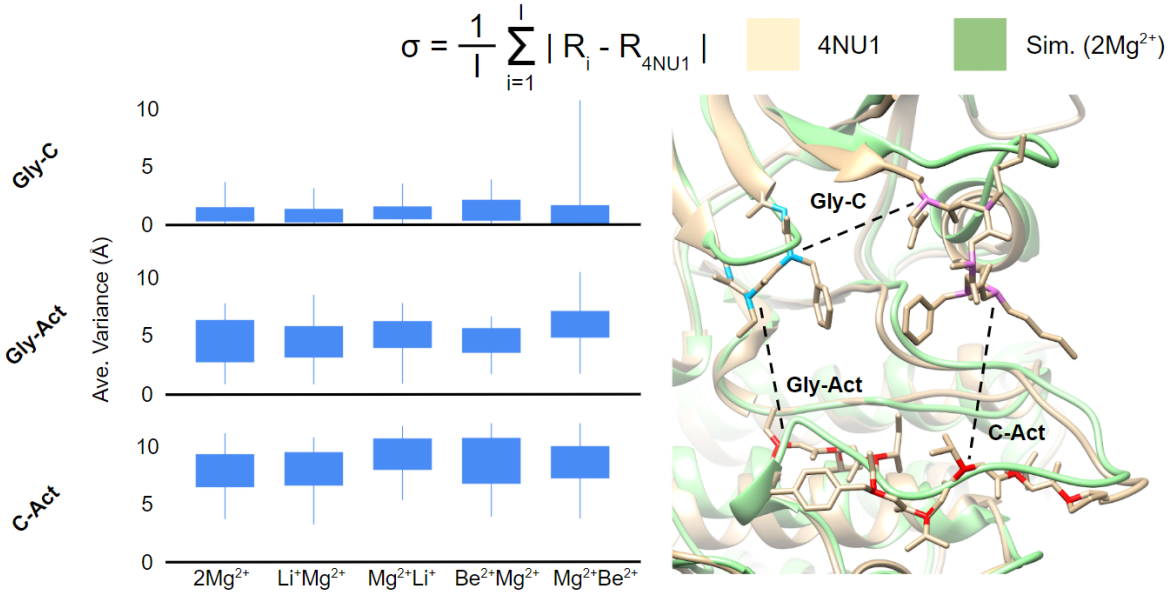

Figure 2: Variance of the peptide binding channel conformation in QM/DMD ensembles from a reference, peptide-bound crystal structure (4NU1). The green structure is an example from the $2Mg^{2+}$ simulations. The average variance for each metal-bound state is graphed on the left with the blue bar spanning one standard deviation above and below the average and the thin blue line showing the minimum and maximum loop distances. The variance was calculated by the equation at the top using the inscribed distances between loops in the picture on the right. The distances used were the minimum distance between any two alpha carbon on opposite loops. I is the number of QM/DMD iterations, R_i is the loop distance in the QM/DMD simulation, and R_{4NU1} is the loop distance in the crystal structure. Note that all the metal bound states report roughly the same variances.

All metal binding affinities in this study were calculated through the recently developed competitive metal affinity (CMA) method,[40] which shows that it can obtain quantitatively accurate relative metal binding affinities compared to experiment.[31,40] This method determines the relative binding affinity to a protein compared to a reference metal using an indirect thermodynamic cycle dependent on experimental metal binding free energies to a chelator. The absolute binding affinities are computationally inaccessible (both resource intensive and error prone) because of the indeterminate structure of solvated metal ions. EDTA was used as a chelator complex for CMA calculations. The first benefit of this complex is that experimental binding affinities are available for nearly all metals, including Mg^{2+}, Li^{+}, and Be^{2+}.[41] Normally the second benefit of EDTA is that its metal-bound structure is known and well behaved: fully coordinating the metal in an octahedral geometry. However, this assumption may not hold for small, low charge metals like the alkali and alkali earth metals of this study. These metals can not satisfy the -4 charge of EDTA alone and so the complex is likely to coordinate additional water molecules – one of the complications that the CMA method seeks to avoid. Indeed, a crystal structure for a Ca^{2+} complex with EDTA shows only partial coordination of the metal with EDTA and a number of closely interacting waters.[42] Nonetheless, CMA binding ΔΔG were calculated using EDTA as the sole ligand in implicit solvent water, as no alternative complex with experimental binding affinities to the examined metals could be found. Free energies for the octahedrally coordinated EDTA complexes were calculated in the same manner as the QM/DMD optimizations but with a dielectric constant of 84 for COSMO to represent the aqueous environment. To mitigate the shortcomings and verify the results using EDTA, an alternative approach using ATP and ADP as chelators was also pursued.

This study also relied on the free energy of exchange of Li^{+} and Be^{2+} from the solvated forms of ATP and ADP to the holoprotein. While they do not offer the same full coordination of EDTA, ATP and ADP are both chelators and recent research has gone into their structure and the position of the water molecules that complete their coordination shells.[43] The solution phase structures used in this study are based on the bimetallic complexes determined recently by Dudev et al. That study did not ascertain structures for Be^{2+}, so the input structures for Be^{2+} are the same as Li^{+}. The Li^{+} input structures were used as both metals prefer tetrahedral geometries while Mg^{2+} adopts an octahedral geometry. The solvated complexes were then fully optimized to account for structural differences and obtain their free energies in the same manner as EDTA, including the use of the COSMO dielectric of 84.

Results and Discussion

Effect of Metals on Substrate Binding Channel: Analysis of the conformational ensembles we generated through QM/DMD for the GSK-3β-ATP form shows no evidence that the metal could alter the nature of peptide/protein substrate binding. To assess this, we calculated the variance of two important features of the protein binding channel from a crystal structure of GSK-3β bound to an axin-derived peptide (PDB ID: 4NU1).[10] While the axin peptide in 4NU1 is different from tau, the binding site should be the same due to the anchoring role the P+4 site plays for pre-phosphorylated substrates. We therefore selected the crystal structure as our reference to see if Li^{+} or Be^{2+} impede the adoption of a structure predisposed to binding. The two geometric features of our analysis are the shape of the binding channel itself as defined by its loops and

$$\sigma = \frac{1}{3\,I}\sum_{i=1}^{I}\sum_{n=3}^{3} \left| R_{n,i} - R_{n,4NU1} \right|$$

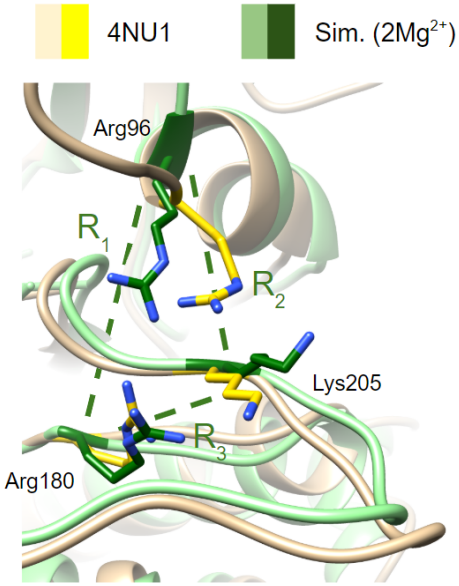

Figure 3: Variance of the P+4 peptide phosphate binding site geometry in QM/DMD ensembles from reference, peptide-bound crystal structure (4NUI). The green structure is an example from a $2Mg^{2+}$ simulation. The variance was calculated using the equation at the top based on distances between the alpha carbon of three positively charged residues that define the P+4 site. I is the number of iterations, $R_{n,i}$ is the distance in the QM/DMD simulation, and $R_{n,4NU1}$ is the distance in the crystal structure.

the structure of the critical P+4 site. If the channel defining loops or the positively charged residues of the P+4 site in the Li^{+} and Be^{2+} states are significantly more distant, this incurs an energetic penalty to pull them together. Furthermore, the greater distance would also make additional binding modes more likely. Together, these changes to the potential energy surface of this event would reduce tau binding affinity.

The variance in the conformation of the peptide channel shows no significant differences between the different metal bound states. We calculated this as the variance from the 4NU1 structure in the distance between the closest alpha carbon for each pair of loops. Our graph depicts the average of this value across all iterations for all replicates of QM/DMD for each metal bound form of GSK-3β (Figure 2). For all the metals, the average variance is small at about 2Å for the Gly-C distance and large, over 5Å, for the distances involving the Act loop. This simply represents the binding channel closing around the peptide upon binding. The variances for the Gly-C loop distance are 0.91 ± 0.57Å for $2Mg^{2+}$, 0.79 ± 0.55Å for $Li^{+}Mg^{2+}$, 1.03 ± 0.51Å for $Mg^{2+}Li^{+}$, 1.26 ± 0.87Å for $Be^{2+}Mg^{2+}$, and 0.66 ± 1.00Å for the $Mg^{2+}Be^{2+}$ form of the protein. The variances for the Gly-Act loop distance are 4.53 ± 1.79Å for $2Mg^{2+}$, 4.47 ± 1.32Å for $Li^{+}Mg^{2+}$, 5.09 ± 1.12Å for $Mg^{2+}Li^{+}$, 4.59 ± 1.03Å for $Be^{2+}Mg^{2+}$, and 5.98 ± 1.12Å for the $Mg^{2+}Be^{2+}$ form of the protein. Finally, the variances for the C-Act loop distance are 7.90 ± 1.39Å for $2Mg^{2+}$, 8.06 ± 1.41Å for $Li^{+}Mg^{2+}$, 9.33 ± 1.32Å for $Mg^{2+}Li^{+}$, 8.75 ± 1.94Å for $Be^{2+}Mg^{2+}$, and 8.64 ± 1.36Å for the $Mg^{2+}Be^{2+}$ form of the protein. However, the difference in the variance between the different metals is small, subsumed by their standard deviations.

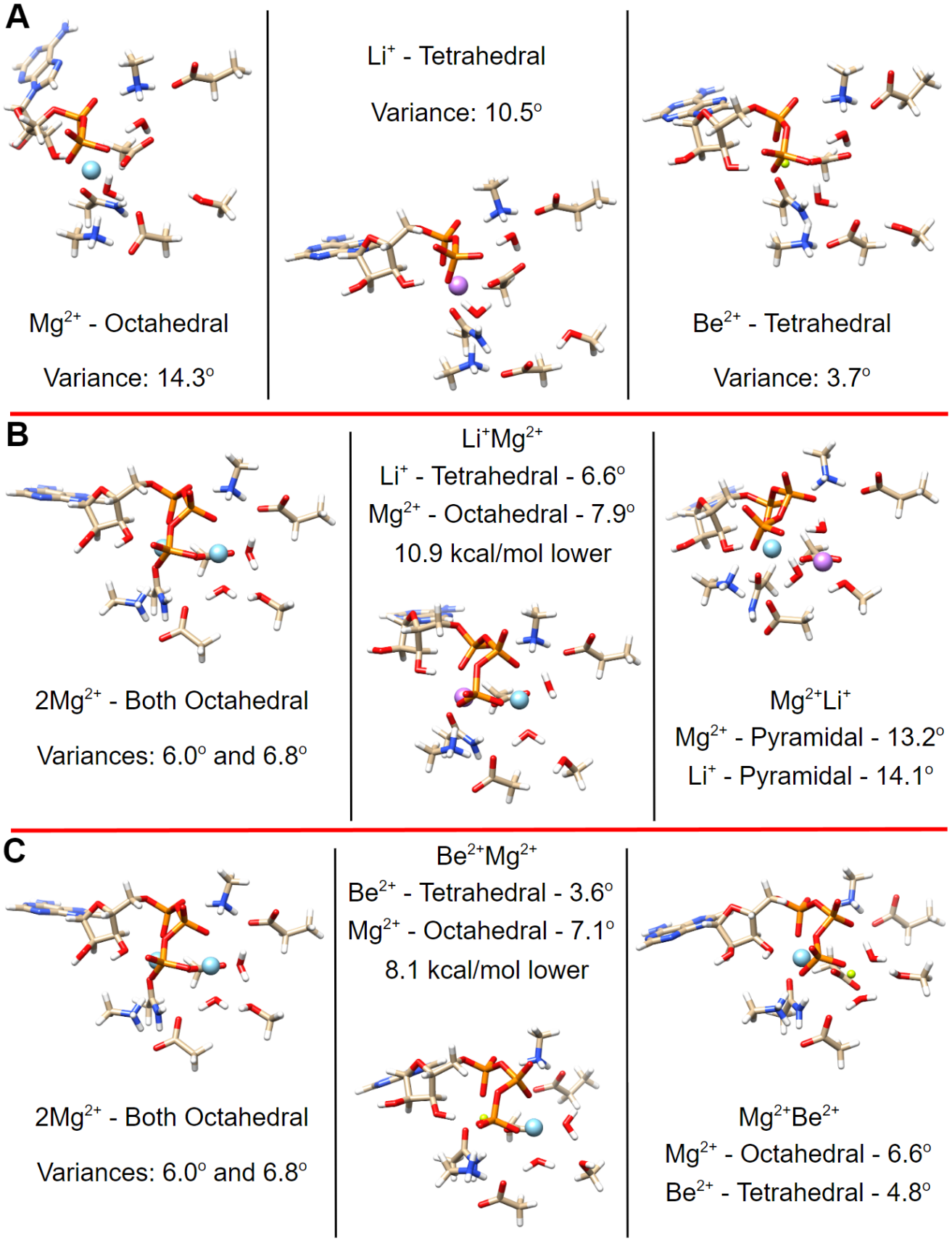

Figure 4: QM optimized geometries of the active site from the QM/DMD simulations for (A) ADP, (B) ATP with Li^+, and (C) ATP with Be^{2+}. Mg^{2+} is shown in cyan, Li^+ in pink, and Be^{2+} in yellow-green. Also reported for each structure are the preferred metal geometries with the average angular variance from ideal angles. The structures from the ATP-bound state also feature the free energy preference for metal substitution at the first binding site over the second. Note that the smaller Li^+ and especially Be^{2+} report much smaller angular variances.

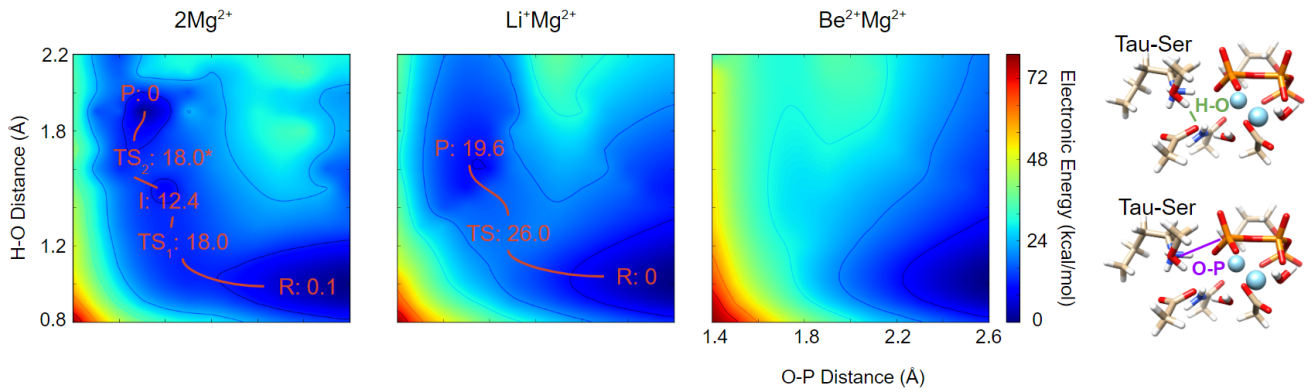

Figure 5: Potential energy surfaces for serine phosphorylation in the native form of GSK and the Li^+ and Be^{2+} bound states. These plots vary the two reaction coordinates: serine hydroxyl hydrogen to aspartate carboxyl oxygen and serine hydroxyl oxygen to ATP terminal phosphorus. Electronic energies are shown as a heat map going from blue (low) to red (high). Stationary points with free energies along the reaction path are recorded in red for the native and Li^+ states. Note how $2Mg^{2+}$ reports two barriers, Li^+ reports one higher one, and Be^{2+} shows no product state and can't perform this reaction by the investigated mechanism.

The shape of the binding channel does not look especially predisposed to protein binding with any metal over the others.

The structure of the P+4 site is similarly invariant between the different metal bound states. As with the channel loops, we calculated the variance from the 4NU1 structure between alpha carbons, this time of Arg96, Arg180, and Lys205. In this case we averaged all three distances together for all iterations of all replicates of QM/DMD for each metal bound state (Figure 3). The variances are all around a small 0.5Å: 0.52 ± 0.25Å for $2Mg^{2+}$, 0.52 ± 0.25Å for Li^+Mg^{2+}, 0.52 ± 0.25Å for $Mg^{2+}Li^+$, 0.52 ± 0.25Å for $Be^{2+}Mg^{2+}$, and 0.57 ± 0.24Å for the $Mg^{2+}Be^{2+}$ form of the protein. As before the differences are minor between the metal states and well below the standard deviation of each ensemble.

Active Site Metal Geometry: The lowest energy active site structures from QM/DMD show significant differences when Li^+ and Be^{2+} bind. The QM calculations suggest that the inhibitory metals preferentially bind to the first binding site closer to the adenosine group. The structures with the inhibitory metals occupying the second, further site are less stable by 10.9 kcal/mol for Li^+ and 8.1 kcal/mol for Be^{2+}. For our future analyses we therefore consider metal substitutions only to the first, apparently dominant site.

Full investigation of the dominant active site structures immediately reveals significant geometric variations between the different metal bound states, dictated by the size and charge of the metal cations. The largest cation is Mg^{2+}, followed by Li^+, and Be^{2+}. This is demonstrated by the average ligand-metal distances which are 2.05 ± 0.06Å for Mg^{2+}, 1.94 ± 0.04Å for Li^+, and 1.64 ± 0.02Å for Be^{2+} in the ADP bound states, and 2.09 ± 0.1Å for Mg^{2+}, 1.95 ± 0.06Å for Li^+, and 1.63 ± 0.04Å for Be^{2+} in the dominant ATP-bound state. Furthemore, both Li^+ and Be^{2+} prefer fewer ligands than Mg^{2+}; they feature tetrahedral coordination with both ATP and ADP, whereas Mg^{2+} is octahedral in both forms (Figure 4). Obviously, the doubly-charged cations attract nucleophilic ligands more strongly, resulting in more favorable electrostatics. On the other hand, smaller cations could favor fewer ligands, benefiting less from metal-ligand electrotactic attraction, but reducing the crowding of the coordination sphere and ligand-ligand repulsion. The total ligand-metal attraction, ligand-ligand repulsion, ligand and and metal coordination strain, and binding site accommodation constitute a complex interplay that we aim to uncover. The resultant interactions in the binding pocket should also contribute to the site thermodynamics.

The joint effects of the metal charge, size, and ligand interactions are reflected in the differences in the strain that these complexes exhibit, judged by the metal angular variance. In the ADP bound state of GSK-3β, the phosphate tail of ADP can better accommodate the coordination of the smaller Li^+ and especially Be^{2+} with less strain than the native Mg^{2+}. In addition, less crowded tetrahedral coordination should have weaker ligand-ligand repulsions and also tighter binding to the metal. In the ADP bound state of GSK-3β the metal angular variances are 14.3° for Mg^{2+}, a smaller 10.5° for Li^+, and only 3.7° for Be^{2+} (Figure 4). Smaller strain is expected to be associated with tighter binding, again featuring Be^{2+} as a strong binder, though the most valid comparison in this case is between Li^+ and Be^{2+}, since both are tetrahedral. A similar trend emerges for the preferred ATP bound states. A notable difference in this case, however, is that Li^+ reports a comparable angular variance of 6.6° to the 6.0° and 6.8° of the native Mg^{2+} structure, while that of Be^{2+} continues to be significantly smaller at 3.6°. Relative to Mg^{2+}, Li^+ coordination appears less strained with ATP than with ADP, which (while being just one of the relevant parameters) can be expected to yield a greater barrier to the catalytic reaction step for Li^+ compared to Mg^{2+}. Be^{2+}, being the tightest binder of both ATP and ADP, should feature specific reactivity as well. Mg^{2+}, while having greater variance, benefits electrostatically from having more ligands in the octahedral sphere, and the exact energetic balance is thus far unclear. The compounding effects of the geometric trends on the thermodynamics of binding and reactivity are evaluated next.

Relative Metal Binding Affinities: Binding affinities that we calculated suggest that Li^+ and Be^{2+} can replace native Mg^{2+} in GSK at various points during its catalytic cycle. When Mg^{2+} is used as the reference metal in our CMA method, the ΔΔG of replacement with Li^+ or Be^{2+} are uniformly negative for the ATP and ADP bound forms of GSK-3β. These values are -16.7 kcal/mol for Li^+ and -38.1 kcal/mol for Be^{2+} in the ADP bound form of the protein and -17.6 kcal/mol for Li^+Mg^{2+}, -6.7 kcal/mol for $Mg^{2+}Li^+$, -23.0 kcal/mol for $Be^{2+}Mg^{2+}$, and -14.9 kcal/mol for $Mg^{2+}Be^{2+}$ in the ATP bound form of the protein. The ΔΔG correspond to the following reactions

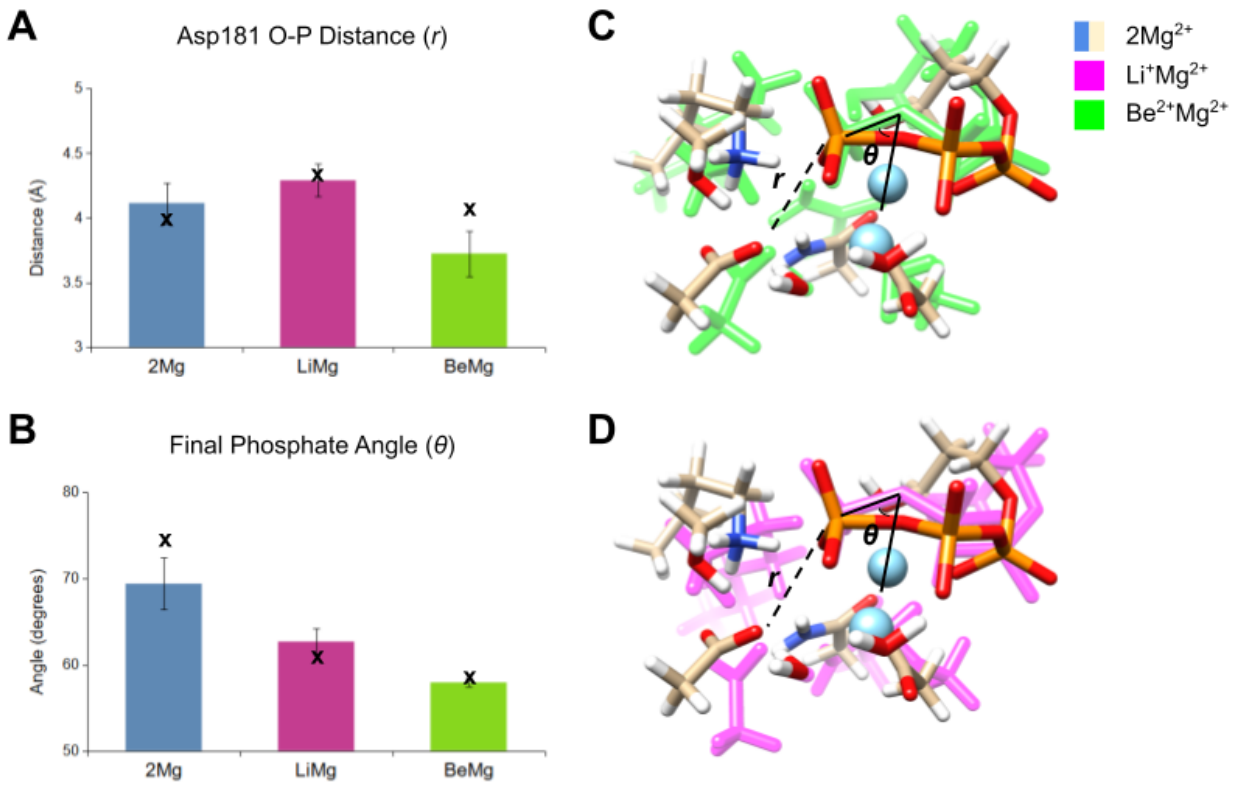

Figure 6: Bar charts of the average and standard deviation of the (A) Asp181 oxygen to final ATP phosphorous distance (r) and (B) final ATP phosphate angle relative to the metal centers (θ) across the full ensemble of structures from the QM/DMD simulations. The values from the phosphorylation reactants are plotted for each state as an 'x'. Blue is the native Mg^{2+} form, magenta the Li^{+} form, and green the Be^{2+} form. The distance r is based on whichever carboxylate oxygen in Asp181 is closest to the final ATP phosphorous in each given structure. The angle θ is inscribed by the vector of the last bridging ATP P-O bond and the vector between the last bridging O and mid-point between the two metals. Note that the values for the phosphorylation reactant Mg^{2+} are distinct from those of the Li^{+} and Be^{2+} states. Both quantities are marked on the structures on the right. Structural deviations of the phosphorylation reactant geometry in the (C) Li^{+} and (D) Be^{2+} bound states are also shown. In both, the native Mg^{2+} geometry is overlaid in tan while the metal substituted geometry is colored pink or green respectively. Note how for both Li^{+} and Be^{2+} the final phosphate group is angled down and away from the tau serine substrate.

$$GSK_{ADP,Mg} + M \rightarrow GSK_{ADP,M} + Mg^{2+} \quad (1)$$

$$GSK_{ATP,2Mg} + M \rightarrow GSK_{ATP,M,Mg} + Mg^{2+} \quad (2)$$

Where M can be either Li^{+} or Be^{2+} and $GSK_{ADP,Mg}$ and $GSK_{ADP,M}$ are the ADP bound form of GSK-3β with Mg^{2+} and the substituted non-native metal in the active site, respectively. This notation carries for equation 2 and all that follow. The uniformly negative competitive metal affinities indicate that Li^{+} and Be^{2+} readily replace Mg^{2+} and bind to GSK more tightly at all considered points during the catalytic cycle. While ambiguities with the EDTA complexes discussed above might contribute to error, these would cancel out when comparing the ADP and ATP states, corresponding to reaction 3:

$$GSK_{ADP,Mg} + GSK_{ATP,M,Mg} \rightarrow GSK_{ADP,M} + GSK_{ATP,2Mg} \quad (3)$$

We see that the ΔΔG between the dominant ATP state and the ADP state is far larger and negative for Be2+ (-15.1 kcal/mol) compared to Li+ (0.9 kcal/mol). As a check, we also calculated the ADP-ATP ΔΔG based on the binding ΔG from the solvated forms of ATP and ADP. Each ΔG calculated this way corresponds to the reactions

$$GSK_{ADP,Mg} + ADP_{M} \rightarrow GSK_{ADP,M} + ADP_{Mg} \quad (4)$$

$$GSK_{ATP,2Mg} + ATP_{M,Mg} \rightarrow GSK_{ATP,M,Mg} + ATP_{2Mg} \quad (5)$$

Therefore, subtracting the binding ΔG for GSK-3β-ATP from GSK-3β-ADP yields energies consistent with the following reaction

$$GSK_{ADP,Mg} + ADP_{M} + GSK_{ATP,M,Mg} + ATP_{2Mg} \rightarrow GSK_{ADP,M} + ADP_{Mg} + GSK_{ATP,2Mg} + ATP_{M,Mg} \quad (6)$$

The results for equation 6 are qualitatively consistent with the earlier EDTA-based CMA approach (equation 3), with +11.9 kcal/mol for Li^{+} and -12.3 kcal/mol for Be^{2+}. Together, our results suggest that Li^{+} has a preference for binding the ATP form of GSK-3β, while Be^{2+} prefers binding to the ADP form. This is consistent with experiment, showing that Li^{+} can not easily bind alongside ADP while Be^{2+} does. The particularly small size and angular variance of Be^{2+}, as well as its greater charge relative to Li^{+}, and better placement of Be^{2+}-bound ADP in the binding pocket all likely contributes to this.

Phosphorylation Reaction Barriers: Analysis of the GSK-3β phosphorylation mechanism shows that Li^{+} inhibition is driven by its direct reduction of the rate of the phosphorylation step itself, as inferred from the geometric differences between Li^{+} and Mg^{2+}. The mechanism involves the deprotonation and phosphorylation of a serine residue either in concert or sequentially. To assess this we calculated potential energy surfaces.

The PES for the tau phosphorylation are shown in Figure 5, and they exhibit significant differences for the three metals. The deep blue wells in the lower right correspond to the reactant states. In the upper left, a well for the product state can be found for Mg^{2+} and Li^{+}. However, the Mg^{2+} and Li^{+} mechanisms are slightly different. The Mg^{2+}-based PES reveals a small well corresponding to an intermediate, whereas for Li^{+} the reaction consists of a single step and has no intermediate. Therefore, the reaction proceeds as SN1 for Mg^{2+} and SN2 for Li^{+}. Furthermore, full optimizations of the stationary points on the PES and frequency calculations yield free energies that suggest a reduced rate of phosphorylation in the Li^{+} bound protein compared to Mg^{2+}. In the native protein the reaction is slightly exothermic, by 0.1 kcal/mol with our level of theory. The highest of its two reaction barriers is a reasonable 17.9 kcal/mol. By contrast in the Li+ case, the reaction is majorly endothermic by 19.6 kcal/mol, and the barrier is 26.0 kcal/mol. This is in line with the qualitative predictions based on the geometries and binding energies of ATP-Li^{+} and ADP-Li^{+} relative to Mg^{2+} forms, presented earlier, and is additionally related to geometric effects in the binding pocket discussed in the next section. Hence, the reaction with Li^{+} is both thermodynamically and kinetically unfavorable, enabling Li^{+} to take an inhibitory role on GSK-3β.

The PES for Be^{2+} shows no well for the product state within the investigated mechanism. This result seems surprising, given that the ADP-Be^{2+} state, the product of this reaction, is very stable and preferred over the ATP-Be^{2+} state (see the Relative Metal Binding Affinities section). However, this is clarified in the next section, where we discuss how structural misalignment of the ATP-Be^{2+} system impedes efficient phosphorylation.

Structural Differences Contributing to Inhibition: The interactions between the metals and the binding pocket of GSK-3β could reveal the structural root of the differences between phosphorylation mechanisms and inform future drug development. The structural features that show the greatest difference between the three considered metal-bound states of GSK-ATP are (i) the distance between the final ATP phosphate group and the oxygen on Asp181 that acts as the base in the reaction and (ii) the angle of the final phosphate group relative to metal centers (Figure 6A-B). We tracked each of these quantities both across the full ensemble of structures generated with QM/DMD and for the phosphorylation reactant structures based on the lowest energy structures from QM/DMD. The Asp181 to final phosphate distance can affect activity. The distance is much smaller for the Mg^{2+} form both on average and for the phosphorylation reactant states than in the Li^{+} form. The Be^{2+} form shows a relatively low distance as well, so its product-less PES likely arises from other quantities. The correlation between activity and the Asp181 distance, at least for Mg^{2+} and Li^{+}, makes sense as Asp181 is the only negatively charged group near the active site that could accept a proton: its greater distance from the substrate Ser and ATP phosphate incurs a greater reaction barrier as the proton or phosphate group must move more over the course of the reaction. In light of our results, we hypothesize that a potential inhibitor which can provide Asp181 with a competing non-covalent interaction would have a similar effect to Li^{+}.

The angle of the final phosphate group correlates fully with activity across the metal bound forms of GSK-3β and likewise yields opportunities for new inhibitors. Both for the phosphorylation reactant structures and the full QM/DMD ensemble, the Mg^{2+} form reports the largest angles, followed by Li^{+}, and finally Be^{2+}. The implications of the angle on the phosphorylation reaction barrier is clear from inspection of the reactant structures. While the final ATP phosphate faces the tau serine substrate with Mg^{2+}, it is shifted slightly down and away from it in the inhibitory structures (Figure 6C-D). This is particularly true of the Be^{2+} active site. This incurs an energetic penalty as the phosphate or tau must move and geometrically reorganize to perform the reaction. In the case of Be^{2+} this penalty appears too large for the reaction to occur at all according to the phosphorylation PES. This is most likely due to the smaller size of Li^{+} and especially Be^{2+}, as they pull the phosphate group toward them with their tighter coordination sphere. Though metal properties appear to drive the final phosphate angle, we suspect any structural changes which shrink that angle would reduce GSK-3β activity, given the resulting poor alignment of the reactant moieties. This might be achieved by crowding of the Gly-C loop, located directly above the ATP binding site.

Finally, based on these structural differences, we put forward a hypothesis regarding the mechanism of Be^{2+} inhibition of GSK-3β. In part, it is not principally different from that of Li^{+}: because Be^{2+} features an even tighter binding of ATP than Li^{+}, the misalignment with the tau serine is also greater, further making the reaction unfavorable. However, Be^{2+} can bind ADP, the product of phosphorylation, even tighter than ATP. While the PES for the reaction suggests that ADP cannot be reached in the Be^{2+} form of the protein, Be^{2+}-ADP could be recruited from solution. Hence, due to very strong binding, both ATP and ADP are predicted to stay bound and inhibit the protein with Be^{2+}, reducing the turnover number of GSK-3β . The opportunity for ADP-based inhibition is accessible only to Be^{2+}, and not to Li^{+}, which constitutes the largest difference in their inhibitory mechanisms. One possible way to check this proposed mechanism would be to bind a small trivalent cation instead of Be^{2+}, to enforce an even tighter binding. No smaller cations than Be^{2+} exist, to the best of our knowledge, but higher valency might still lead to a similar effect.

Conclusion: GSK-3β is an important, but challenging, target for treating neurological and psychiatric disorders. Atomic-scale information about the effect of rare, successful inhibitors is helpful to design new inhibitory drugs. In this study, we identified how Li^{+} affects GSK-3β structure to inhibit its activity and how this contrasts with another metal ion inhibitor, Be^{2+}. Li^{+} binds most strongly to the ATP bound form of GSK-3β and directly increases the barrier for the phosphorylation reaction through poor orientation of the transferring final phosphate group. This differs from Be^{2+}, which binds ATP tighter than Li+ does and can also tightly bind ADP. The bound ATP is so strongly attracted to the compact and highly-charged Be^{2+} that it becomes too contorted and out of alignment with the rest of the binding site to undergo subsequent phosphorylation. If the protein recruits Be^{2+} alongside ADP, then this binding is even stronger. We therefore conclude that Be^{2+} stays bound to the protein either with unreacted ATP or ADP. In the case of both metals, their inhibitory effect arises from their small ionic radii relative to the native Mg^{2+}, exacerbated in Be^{2+} by its comparably high charge. While these are metallic properties, a similar effect might be achieved by new therapeutics that provide competing interactions to an Asp181 residue that acts as the base during phosphorylation or crowding the final ATP phosphate group.

ASSOCIATED CONTENT

Supporting Information is available free of charge via the Internet at http://pubs.acs.org.

AUTHOR INFORMATION

Corresponding Authors

*E-mail: arrafzaher@campus.technion.ac.il
**E-mail: ana@chem.ucla.edu. Phone: +1 310 8253769

Funding Sources

Financial support comes from the NSF CHE-1903808 grant to A.N.A. We also acknowledge UCLA-IDRE and XSEDE for providing computational resources.

Notes

We declare no competing financial interest.

ACKNOWLEDGMENT

We thank the Institute for Digital Research and Education at UCLA and the Extreme Science and Engineering Discovery Environment for supercomputer time.

ABBREVIATIONS

GSK-3β, glycogen synthase kinase 3β; BD, bipolar disorder; AD, Alzheimer's disease; MAPK, mitogen-activated protein kinase; CDK, cyclin-dependent kinase; PKA, protein kinase A; PKC, protein kinase C; DFT, density functional theory;

REFERENCES

(1) Lei, P.; Ayton, S.; Bush, A. I.; Adlard, P. A. GSK-3 in Neurodegenerative Diseases. *Int. J. Alzheimer's Dis.* **2011**, *2011*.

(2) Lin, R.; Jones, N. C.; Kwan, P. Unravelling the Role of Glycogen Synthase Kinase-3 in Alzheimer's Disease-Related Epileptic Seizures. *Int. J. Mol. Sci.* **2020**, *21* (10), 3676.

(3) Hooper, C.; Killick, R.; Lovestone, S. The GSK3 Hypothesis of Alzheimer's Disease. *J. Neurochem.* **2008**, *104* (6), 1433–1439.

(4) King, M. K.; Pardo, M.; Cheng, Y.; Downey, K.; Jope, R. S.; Beurel, E. Glycogen Synthase Kinase-3 Inhibitors: Rescuers of Cognitive Impairments. *Pharmacol. Ther.* **2014**, *141* (1), 1–12.

(5) Aourz, N.; Serruys, A.-S. K.; Chabwine, J. N.; Balegamire, P. B.; Afrikanova, T.; Edrada-Ebel, R.; Grey, A. I.; Kamuhabwa, A. R.; Walrave, L.; Esguerra, C. V. Identification of GSK-3 as a Potential Therapeutic Entry Point for Epilepsy. *ACS Chem. Neurosci.* **2018**, *10* (4), 1992–2003.

(6) Morales-García, J. A.; Susín, C.; Alonso-Gil, S.; Pérez, D. I.; Palomo, V.; Pérez, C.; Conde, S.; Santos, A.; Gil, C.; Martínez, A. Glycogen Synthase Kinase-3 Inhibitors as Potent Therapeutic Agents for the Treatment of Parkinson Disease. *ACS Chem. Neurosci.* **2013**, *4* (2), 350–360.

(7) Davies, M. P.; Benitez, R.; Perez, C.; Jakupovic, S.; Welsby, P.; Rzepecka, K.; Alder, J.; Davidson, C.; Martinez, A.; Hayes, J. M. Structure-Based Design of Potent Selective Nanomolar Type-II Inhibitors of Glycogen Synthase Kinase-3β. *J. Med. Chem.* **2021**, *64* (3), 1497–1509.

(8) Eldar-Finkelman, H.; Martinez, A. GSK-3 Inhibitors: Preclinical and Clinical Focus on CNS. *Front. Mol. Neurosci.* **2011**, *4*, 32.

(9) Bhat, R. V; Andersson, U.; Andersson, S.; Knerr, L.; Bauer, U.; Sundgren-Andersson, A. K. The Conundrum of GSK3 Inhibitors: Is It the Dawn of a New Beginning? *J. Alzheimer's Dis.* **2018**, *64* (s1), S547–S554.

(10) Stamos, J. L.; Chu, M. L.-H.; Enos, M. D.; Shah, N.; Weis, W. I. Structural Basis of GSK-3 Inhibition by N-Terminal Phosphorylation and by the Wnt Receptor LRP6. *Elife* **2014**, *3*, e01998.

(11) Palomo, V.; Soteras, I.; Perez, D. I.; Perez, C.; Gil, C.; Campillo, N. E.; Martinez, A. Exploring the Binding Sites of Glycogen Synthase Kinase 3. Identification and Characterization of Allosteric Modulation Cavities. *J. Med. Chem.* **2011**, *54* (24), 8461–8470.

(12) Arfeen, M.; Bharatam, P. V. Design of Glycogen Synthase Kinase-3 Inhibitors: An Overview on Recent Advancements. *Curr. Pharm. Des.* **2013**, *19* (26), 4755–4775.

(13) Cade, J. F. J. Lithium Salts in the Treatment of Psychotic Excitement. *Med. J. Aust.* **1949**.

(14) Hampel, H.; Ewers, M.; Bürger, K.; Annas, P.; Mörtberg, A.; Bogstedt, A.; Frölich, L.; Schröder, J.; Schönknecht, P.; Riepe, M. W. Lithium Trial in Alzheimer's Disease: A Randomized, Single-Blind, Placebo-Controlled, Multicenter 10-Week Study. *J. Clin. Psychiatry* **2009**, *70* (6), 922–931.

(15) Leyhe, T.; Eschweiler, G. W.; Stransky, E.; Gasser, T.; Annas, P.; Basun, H.; Laske, C. Increase of BDNF Serum Concentration in Lithium Treated Patients with Early Alzheimer's Disease. *J. Alzheimer's Dis.* **2009**, *16* (3), 649–656.

(16) Breen, M. S.; White, C. H.; Shekhtman, T.; Lin, K.; Looney, D.; Woelk, C. H.; Kelsoe, J. R. Lithium-Responsive Genes and Gene Networks in Bipolar Disorder Patient-Derived Lymphoblastoid Cell Lines. *Pharmacogenomics J.* **2016**, *16* (5), 446–453.

(17) Ryves, W. J.; Harwood, A. J. Lithium Inhibits Glycogen Synthase Kinase-3 by Competition for Magnesium. *Biochem. Biophys. Res. Commun.* **2001**, *280* (3), 720–725.

(18) Ryves, W. J.; Dajani, R.; Pearl, L.; Harwood, A. J. Glycogen Synthase Kinase-3 Inhibition by Lithium and Beryllium Suggests the Presence of Two Magnesium Binding Sites. *Biochem. Biophys. Res. Commun.* **2002**, *290* (3), 967–972.

(19) Fountoulakis, K. N.; Vieta, E.; Bouras, C.; Notaridis, G.; Giannakopoulos, P.; Kaprinis, G.; Akiskal, H. A Systematic Review of Existing Data on Long-Term Lithium Therapy: Neuroprotective or Neurotoxic? *Int. J. Neuropsychopharmacol.* **2008**, *11* (2), 269–287.

(20) Schou, M. Lithium Treatment at 52. *J. Affect. Disord.* **2001**, *67* (1–3), 21–32.

(21) Cheng, Y.; Zhang, Y.; McCammon, J. A. How Does the CAMP-Dependent Protein Kinase Catalyze the Phosphorylation Reaction: An Ab Initio QM/MM Study. *J. Am. Chem. Soc.* **2005**, *127* (5), 1553–1562.

(22) Gerlits, O.; Tian, J.; Das, A.; Langan, P.; Heller, W. T.; Kovalevsky, A. Phosphoryl Transfer Reaction Snapshots in Crystals: Insights into the Mechanism of Protein Kinase a Catalytic Subunit. *J. Biol. Chem.* **2015**, *290* (25), 15538–15548.

(23) Dudev, T.; Lim, C. Competition between Li+ and Mg2+ in Metalloproteins. Implications for Lithium Therapy. *J. Am. Chem. Soc.* **2011**, *133* (24), 9506–9515.

(24) Sun, H.; Jiang, Y.; Yu, Q.; Luo, C.; Zou, J. The Effect of Li+ on GSK-3 Inhibition: Molecular Dynamics Simulation. *J. Mol. Model.* **2011**, *17* (2), 377–381.

(25) Lu, S.-Y.; Jiang, Y.-J.; Zou, J.-W.; Wu, T.-X. Dissection of the Difference between the Group I Metal Ions in Inhibiting GSK3β: A Computational Study. *Phys. Chem. Chem. Phys.* **2011**, *13* (15), 7014–7023.

(26) Sparta, M.; Shirvanyants, D.; Ding, F.; Dokholyan, N. V; Alexandrova, A. N. Hybrid Dynamics Simulation Engine for Metalloproteins. *Biophys. J.* **2012**, *103* (4), 767–776.

(27) Ding, F.; Tsao, D.; Nie, H.; Dokholyan, N. V. Ab Initio Folding of Proteins with All-Atom Discrete Molecular Dynamics. *Structure* **2008**, *16* (7), 1010–1018.

(28) Proctor, E. A.; Ding, F.; Dokholyan, N. V. Discrete Molecular Dynamics. *Wiley Interdiscip. Rev. Comput. Mol. Sci.* **2011**, *1* (1), 80–92.

(29) Sparta, M.; Valdez, C. E.; Alexandrova, A. N. Metal-Dependent Activity of Fe and Ni Acireductone Dioxygenases: How Two Electrons Reroute the Catalytic Pathway. *J. Mol. Biol.* **2013**, *425* (16), 3007–3018.

(30) Nechay, M. R.; Gallup, N. M.; Morgenstern, A.; Smith, Q. A.; Eberhart, M. E.; Alexandrova, A. N. Histone Deacetylase 8: Characterization of Physiological Divalent Metal Catalysis. *J. Phys. Chem. B* **2016**, *120* (26), 5884–5895.

(31) Reilley, D. J.; Fuller III, J. T.; Nechay, M. R.; Victor, M.; Li, W.; Ruberry, J. D.; Mujika, J. I.; Lopez, X.; Alexandrova, A. N. Toxic and Physiological Metal Uptake and Release by Human Serum Transferrin. *Biophys. J.* **2020**, *118* (12), 2979–2988.

(32) Valdez, C. E.; Morgenstern, A.; Eberhart, M. E.; Alexandrova, A. N. Predictive Methods for Computational Metalloenzyme Redesign–a Test Case with Carboxypeptidase A. *Phys. Chem. Chem. Phys.* **2016**, *18* (46), 31744–31756.

(33) Reilley, D. J.; Popov, K. I.; Dokholyan, N. V; Alexandrova, A. N. Uncovered Dynamic Coupling Resolves the Ambiguous Mechanism of Phenylalanine Hydroxylase Oxygen Binding. *J. Phys. Chem. B* **2019**, *123* (21), 4534–4539.

(34) Valdez, C. E.; Sparta, M.; Alexandrova, A. N. The Role of the Flexible L43-S54 Protein Loop in the CcrA Metallo-β-Lactamase in Binding Structurally Dissimilar β-Lactam Antibiotics. *J. Chem. Theory Comput.* **2013**, *9* (1), 730–737.

(35) Furche, F.; Ahlrichs, R.; Hättig, C.; Klopper, W.; Sierka, M.; Weigend, F. Turbomole. *Wiley Interdiscip. Rev. Comput. Mol. Sci.* **2014**, *4* (2), 91–100.

(36) Staroverov, V. N.; Scuseria, G. E.; Tao, J.; Perdew, J. P. Comparative Assessment of a New Nonempirical Density Functional: Molecules and Hydrogen-Bonded Complexes. *J. Chem. Phys.* **2003**, *119* (23), 12129–12137.

(37) Grimme, S.; Antony, J.; Ehrlich, S.; Krieg, H. A Consistent and Accurate Ab Initio Parametrization of Density Functional Dispersion Correction (DFT-D) for the 94 Elements H-Pu. *J. Chem. Phys.* **2010**, *132* (15), 154104.

(38) Weigend, F.; Ahlrichs, R. Balanced Basis Sets of Split Valence, Triple Zeta Valence and Quadruple Zeta Valence Quality for H to Rn: Design and Assessment of Accuracy. *Phys. Chem. Chem. Phys.* **2005**, *7* (18), 3297–3305.

(39) Klamt, A. Conductor-like Screening Model for Real Solvents: A New Approach to the Quantitative Calculation of Solvation Phenomena. *J. Phys. Chem.* **1995**, *99* (7), 2224–2235.

(40) Reilley, D. J.; Hennefarth, M. R.; Alexandrova, A. N. The Case for Enzymatic Competitive Metal Affinity Methods. *ACS Catal.* **2020**, *10* (3), 2298–2307.

(41) Anderegg, G. *Critical Survey of Stability Constants of EDTA Complexes: Critical Evaluation of Equilibrium Constants in Solution: Stability Constants of Metal Complexes*; Elsevier, 2013.

(42) Barnett, B. L.; Uchtman, V. A. Structural Investigations of Calcium-Binding Molecules. 4. Calcium Binding to Aminocarboxylates. Crystal Structures of Ca (CaEDTA). 7H2O and Na (CaNTA). *Inorg. Chem.* **1979**, *18* (10), 2674–2678.

(43) Dudev, T.; Grauffel, C.; Lim, C. How Native and Alien Metal Cations Bind ATP: Implications for Lithium as a Therapeutic Agent. *Sci. Rep.* **2017**, *7* (1), 1–10.